ACS OMEGA

Article

Cite This: ACS Omega 2019, 4, 765−774

http://pubs.acs.org/journal/acsodf

Enhancing Luminescence and X-ray Absorption Capacity of Eu^{3+}:LaF_3 Nanoparticles by Bi^{3+} Codoping

Daniel González Mancebo,[†] Ana Isabel Becerro,*[,†] Ariadna Corral,[‡] María Moros,[§] Marcin Balcerzyk,[‡] Jesús M. de la Fuente,[§] and Manuel Ocaña[†]

[†]Instituto de Ciencia de Materiales de Sevilla (CSIC-US), c/Américo Vespucio, 49, 41092 Seville, Spain

[‡]Centro Nacional de Aceleradores (US, JA, CSIC), Seville 41092, Spain

[§]Instituto de Ciencia de Materiales de Aragón, CSIC/University of Zaragoza, and CIBER-BBN, Edificio I+D, C/Mariano Esquillor s/n, 50018 Zaragoza, Spain

Supporting Information

ABSTRACT: Bi^{3+} codoping has been proposed in this work with a twofold objective, namely, enhancing the luminescence emission of Eu^{3+}:LaF_3 nanoparticles (NPs) and increasing their X-ray attenuation capacity, with the purpose of obtaining a bimodal bioprobe for luminescence bioimaging and X-ray computed tomography. The synthesis method, reported here for the first time for LaF_3 particles, allowed obtaining uniform, nonaggregated NPs using a homogeneous precipitation in polyol medium at room temperature in just 2 h. The simplicity of the synthesis method allows the large-scale production of NPs. LaF_3 NPs with different Eu^{3+} contents were first synthesized to find the critical Eu^{3+} concentration, producing the highest emission intensity. This concentration was subsequently used to fabricate Bi^{3+}−Eu^{3+}-codoped LaF_3 NPs using the same method. The emission intensity of the codoped NPs increased in more than one order of magnitude, thanks to the possibility of excitation through the Bi^{3+} → Eu^{3+} energy-transfer band. The luminescence properties of the codoped NPs were analyzed in detail to find the mechanism responsible for the emission enhancement. Finally, it was demonstrated that the high atomic number of Bi^{3+}, higher than that of lanthanides, was an added value of the material because it increased its X-ray attenuation capacity. In summary, the LaF_3 NPs codoped with Eu^{3+} and Bi^{3+} presented in this work are promising candidates as a bimodal bioprobe for luminescence bioimaging and X-ray computed tomography.

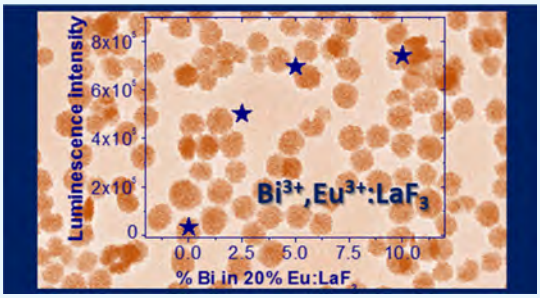

1. INTRODUCTION

Among luminescent materials, lanthanide (Ln^{3+})-doped inorganic nanophosphors (Ln:phosphors) have evoked considerable attention in the last decades in many fields, including optoelectronics and optical bioimaging.[1,2] Compared with the conventional organic dyes and semiconductor quantum dots, Ln:phosphors possess high thermal and chemical stability, low toxicity, and many superior luminescence features, such as large Stokes shifts, narrow emission bands, and long lifetimes. Ln:phosphors based on fluoride matrices show an additional advantage related with the low phonon energy of the fluoride lattice, which minimizes nonradiative deactivation through multiphonon−photon interactions, thus providing improved quantum efficiency to the phosphor.[3] Ln:phosphors suffer, however, from an important drawback related to the forbidden character of the 4f−4f transitions in Ln^{3+} ions, which results in a low-emission intensity. Different strategies have been developed to overcome this inconvenience including energy transfer from the host matrix to the doping Ln^{3+} ion or the approach based on the sensitizer−activator pair. The first strategy has been reported for a large number of Ln-based hosts such as vanadates,[4] tungstates,[5,6] molybdates,[7,8] and so on. However, it is not valid for fluorides, whose importance related to their low phonon energy has been commented above. Therefore, a more appropriate strategy to enhance lanthanide emission in lanthanide fluoride-based phosphors is based on the sensitizer−activator pair. The sensitizer serves the function of energy donor, absorbing the radiation and cooperatively transferring it to the activator. It is well-known, for example, that Bi^{3+} can act as a sensitizer to enhance lanthanide (Eu^{3+}, Tb^{3+}, Sm^{3+}, and Dy^{3+}) emissions, through Bi^{3+} → Ln^{3+} energy transfer in different Ln-based hosts.[9−15] However, very few reports have been devoted to the Bi^{3+} → Ln^{3+} energy-transfer process in Bi^{3+},Ln^{3+} codoped fluorides. To the best of our knowledge, the only related fluoride system reported is YF_3:Eu^{3+},Bi^{3+} although the analysis of the Bi^{3+} → Eu^{3+} energy-transfer process in the material does not seem to be correct because of the clear contamination of the nominally Eu^{3+} free sample with Eu^{3+}.[16]

Received: November 13, 2018
Accepted: December 26, 2018
Published: January 9, 2019

DOI: 10.1021/acsomega.8b03160
ACS Omega 2019, 4, 765−774

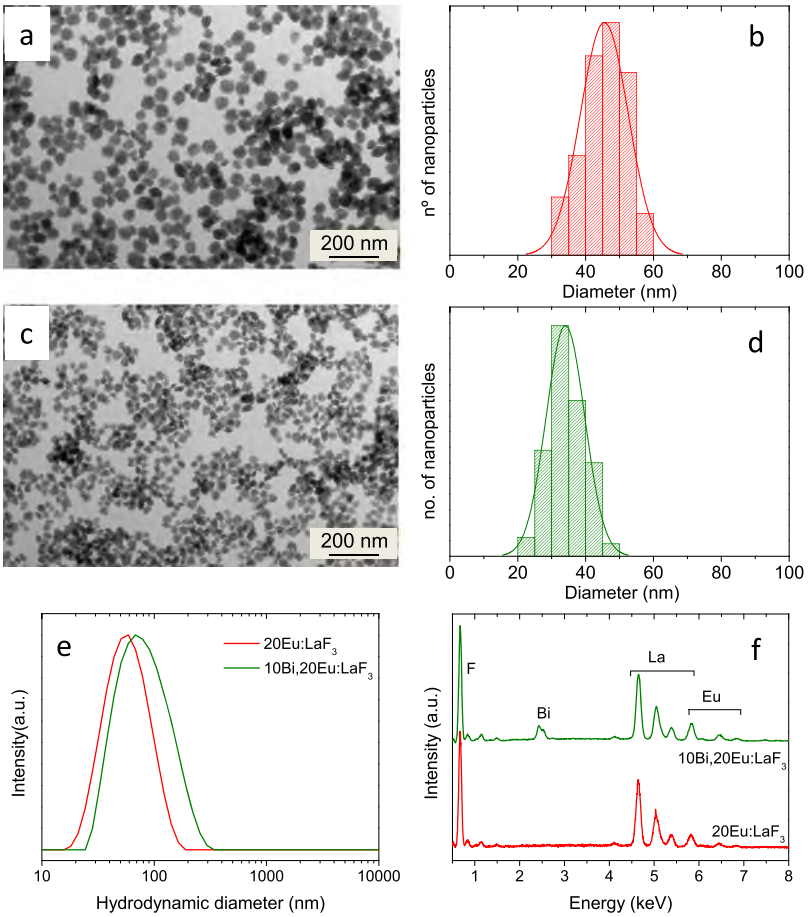

Figure 1. (a,b) TEM micrograph of LaF_3 NPs doped with 20 mol % Eu^{3+} and the corresponding histogram showing size distribution. (c,d) TEM micrograph of LaF_3 NPs codoped with 10 mol % Bi^{3+} and 20 mol % Eu^{3+} and corresponding histogram showing size distribution. (e) DLS plots showing hydrodynamic diameter distribution of NPs shown in (a,c). (f) EDX spectra recorded under the SEM of NPs shown in (a,c).

On the other hand, because of the high atomic number (Z) of lanthanides (Z = 57−71), Ln:phosphors have additionally been proposed as contrast agents for X-ray computed tomography (CT) in medical diagnosis.[17] Codoping with Bi^{3+} is, therefore, not only interesting for the Ln^{3+} emission enhancement but also because the high atomic number of Bi (Z = 83) is expected to increase the X-ray attenuation capacity of the material and, consequently, the contrast in the CT image. In summary, we hypothesize that Bi,Ln codoped fluorides could be excellent candidates as bifunctional bioprobes for optical bioimaging and CT. It should be noted that for these applications, such materials must consist of uniform nanoparticles (NPs)[18] because the size and shape of the materials may strongly affect their physical properties, including luminescence and the interaction with cells and living organisms.[19] In addition, such NPs must be nontoxic and present high colloidal stability in aqueous media.

Herein, we report the synthesis of a red phosphor with high intensity emission consisting of highly dispersed Bi^{3+},Eu^{3+} codoped LaF_3 NPs with uniform size and shape and low toxicity, which has potential applications for bioimaging. Lanthanum has been chosen as the cation of the fluoride matrix cation because of the identical ionic radius of La^{3+} and Bi^{3+} (1.03 Å in VI coordination), which guarantees the doping process and avoids structural or morphological modifications of the resultant material. We have followed a very simple and quick synthesis method based on the coprecipitation of cations and fluoride ions in a mixture of ethylene glycol (EG) and water at room temperature, that had never been used before for LaF_3-based NPs. In a previous paper, we have shown that this method proved to be successful for the synthesis of CeF_3 NPs,[20] and it is expected to be also useful for the synthesis of LaF_3 NPs because of similar characteristics of both Ce^{3+} and La^{3+} ions. This synthesis method is clearly advantageous versus the other methods reported in the literature for LaF_3 NPs, which require the use of either high temperatures[21,22] or additives[23,24] to get uniform, nonaggregated NPs. The study involves the synthesis of LaF_3 NPs singly doped with Eu^{3+} and Bi^{3+} and codoped with Eu^{3+} and Bi^{3+} to find the doping contents producing the maximum emission intensity and to eventually understand the $Bi^{3+} \rightarrow Eu^{3+}$ energy-transfer process in the codoped phosphor. Finally, the X-ray absorption properties of Bi,Eu:LaF_3 NPs were studied to demonstrate their additional potential as X-ray CT contrast agents.

2. RESULTS AND DISCUSSION

2.1. Morphology, Microstructure, Crystalline Structure, and Colloidal Stability of Eu-Doped and Eu,Bi-Codoped LaF_3 NPs. The following strategy has been followed to find the LaF_3 doping contents producing the maximum emission intensity. LaF_3 NPs doped with different Eu^{3+} concentrations (hereafter called xEu:LaF_3 NPs, where x refers to the mol % Eu^{3+}) were first synthesized to find the Eu^{3+} content that produces the maximum emission intensity. NPs

DOI: 10.1021/acsomega.8b03160
ACS Omega 2019, 4, 765−774

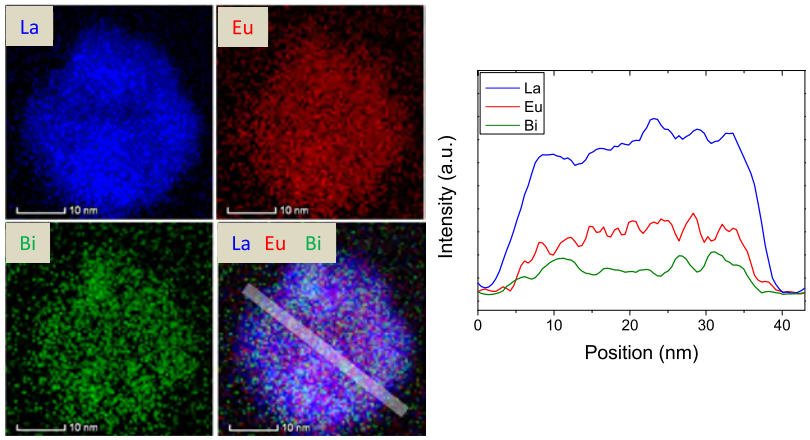

Figure 2. Left: EDX mappings, recorded under the TEM, showing uniform distribution of La, Eu, and Bi in LaF_3 NPs doped with 10 mol % Bi^{3+} and 20 mol %Eu^{3+}. Right: EDX profile across the line marked on the merged La, Eu, and Bi mapping shown on the left.

doped with the optimum Eu content and codoped with different Bi concentrations (hereafter called *x*Bi,20Eu:LaF_3 NPs, where *x* refers to the mol % Bi^{3+}) were subsequently prepared to optimize the Bi^{3+} content in the codoped Eu,Bi LaF_3 phosphor.

It is well-known that uniform particles can be obtained by coprecipitation through a slow and controlled release of the precipitating anions or cations in the reaction medium.[25] We have used, in the present study, a strategy based on the slow release of fluoride anions by the hydrolysis of $NaBF_4$,[20] whereas lanthanum, europium, and bismuth ions were freely released in the reaction medium by dissolution of their nitrate salts. EG mixed with a small volume of water (90/10 volume ratio) was selected as a solvent because polyols have been amply shown to act as both solvent and capping agents, thus limiting the particle growth.[26] The small portion of water in the reaction medium is intended to promote the $NaBF_4$ hydrolysis.

Figure 1a shows the transmission electron microscope (TEM) image of the 20Eu:LaF_3 NPs obtained, following the synthesis protocol described above. The NPs exhibit a rounded morphology with an average diameter of 45 nm (histogram shown in Figure 1b). This is also the morphology and size exhibited by the NPs obtained for any Eu^{3+} content [scanning electron microscope (SEM) images of *x*Eu:LaF_3 with *x* = 2.5, 5, 10, 20, and 30 are shown in Figure S1]. The synthetic protocol was also useful to obtain uniform LaF_3 NPs codoped with 20% Eu^{3+} and variable Bi^{3+} contents. The resulting NPs also showed a rounded shape although their mean diameter decreased with increasing Bi^{3+} content (Figure S2), so that rounded NPs with an average diameter of 35 nm (Figure 1c,d) were obtained for the 10Bi,20Eu:LaF_3 composition, which corresponds to the highest Bi^{3+} content analyzed in this work. The average hydrodynamic diameter obtained from dynamic light scattering (DLS) measurements for aqueous suspensions of the 20Eu:LaF_3 NPs (Figure 1e) was 55 nm, indicating that they were well-dispersed in water, most probably because of the high value of the zeta potential (+36 mV) measured (at pH = 5.4) for such dispersions, which must cause an electrostatic repulsion between particles. A slight degree of aggregation was, however, detected for the 10Bi,20Eu:LaF_3 NPs (Figure 1e) as revealed by their hydrodynamic diameter (61 nm), probably as a consequence of the lower zeta potential (+25 mV) measured for this sample. Nevertheless, such an average diameter was well inside the nanometer range meeting the size criteria required for bioapplications.

Energy-dispersive X-ray (EDX) spectra recorded under SEM (EDX/SEM) on the Eu-doped and Eu,Bi-codoped NPs evidenced the presence of the doping ions in all compositions. Thus, Eu peaks were detected in the 20Eu:LaF_3 NPs in addition to La and F, whereas both Eu and Bi signals could be observed in the spectra of the 10Bi,20Eu:LaF_3 NPs, as shown in Figure 1f. On the other hand, Eu and Bi compositional maps recorded under TEM on an individual NP with nominal 10Bi,20Eu:LaF_3 composition are shown in Figure 2, together with the EDX analyses recorded along the line plotted on the map showing the distribution of all three elements. Both the compositional maps and the profile line show a homogeneous distribution of elements, with no signs of segregation.

The Eu:LaF_3 samples were crystallized into the hexagonal system at any Eu^{3+} doping level, as is the case of the pristine LaF_3 structure. Reflections were observed in the X-ray diffraction (XRD) patterns of different Eu-containing LaF_3 samples (Figure 3a) shifted toward higher 2θ values with increasing Eu content, whereas codoping the 20Eu:LaF_3 composition with Bi^{3+} did not, however, produce any shifting of the XRD peaks whatever the Bi content was (Figure 3b). To understand the origin of such diffraction peaks behavior, the unit cell volume of the Eu:LaF_3 and Bi,Eu:LaF_3 samples has been calculated by Rietveld refinement from the corresponding XRD patterns using TOPAS software. The values obtained have been plotted versus Eu^{3+} content for Eu:LaF_3 samples (Figure 3c, left panel) and versus Bi content for *x*Bi,20Eu:LaF_3 samples (Figure 3c, right panel). The unit cell volume decreases with increasing Eu^{3+} content in Eu:LaF_3, which indicates the effective replacement of La^{3+} (ionic radius = 1.03 Å in VI coordination, which is the coordination of the lanthanide ion in hexagonal lanthanide trifluorides) with Eu^{3+} (0.947 Å in VI coordination) in the LaF_3 unit cell. On the other hand, no appreciable change is observed in the unit cell volume of the *x*Bi,20Eu:LaF_3 system with increasing Bi^{3+} content, which would be in agreement with the replacement of La^{3+} with Bi^{3+} given the identical ionic radius of both of them in VI coordination (1.03 Å). The width of the reflections did not change with doping content in any of the Eu-doped and Bi,Eu-codoped samples. The crystallite size calculated from the width of the (111) reflection using Scherrer equation was ~11 nm, which is smaller than the NP size derived from

DOI: 10.1021/acsomega.8b03160
ACS Omega 2019, 4, 765−774

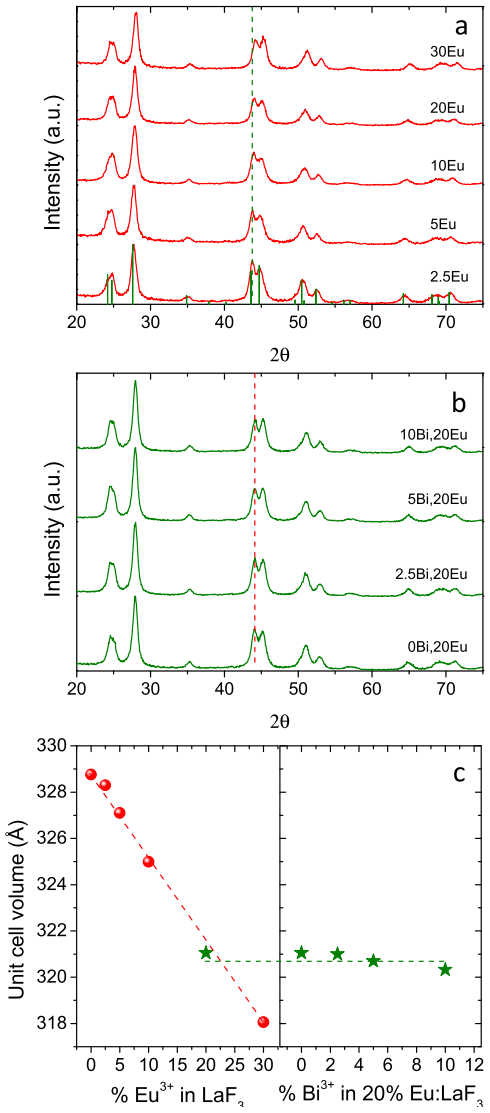

Figure 3. XRD patterns of (a) LaF_3 NPs doped with different Eu^{3+} contents (mol % Eu shown on the labels), (b) LaF_3 NPs codoped with 20 mol % Eu^{3+} and different Bi^{3+} contents (mol % Bi^{3+} shown in the labels), and (c) unit cell volume versus Eu^{3+} and Bi^{3+} contents in Eu:LaF_3 NPs (red circles) and Bi,20Eu:LaF_3 NPs (green stars), respectively. Straight dashed lines are linear fits to the data.

the TEM and SEM micrographs shown above. This result indicates that NPs are polycrystalline in character, and the formation mechanism might involve the self-assembling of subunits to eventually shape the observed NPs. The NP microstructure was further analyzed in detail by TEM and electron diffraction to confirm their polycrystalline character and to obtain information about the orientation of the constituting subunits. The 10Bi,20Eu:LaF_3 composition has been selected for this study, as this is the sample with the best luminescence and X-ray attenuation properties, as will be presented later in this work. Figure 4a shows the HREM micrograph of a single NP, where the individual subunits can be easily observed. The fast Fourier transform (FFT) pattern (Figure 4b) calculated from the individual crystallite shown in the square region of Figure 4a exhibits individual spots that are compatible with a hexagonal single crystal, as corresponds to LaF_3. A very similar FFT pattern (Figure 4c) was obtained from the whole NP although, in this case, the spots are

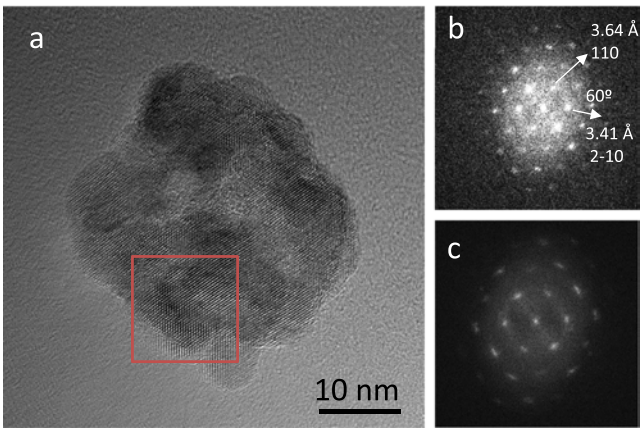

Figure 4. (a) TEM micrograph of an individual LaF_3 NP codoped with 10 mol % Bi^{3+} and 20 mol % Eu^{3+}. (b) FFT pattern calculated from the square region marked in (a). (c) FFT pattern calculated using the whole NP.

elongated indicating a slight degree of misorientation of the subunits forming the NP.

2.2. Luminescence Properties of Eu^{3+}-Doped, Bi^{3+}-Doped, and Bi^{3+},Eu^{3+}-Codoped LaF_3 NPs. *2.2.1. Optimum Eu^{3+}-Doping Level in Eu:LaF_3 NPs.* It is well-known that the luminescence of doped materials depends on the concentration of emitting centers and their interaction with luminescence killers (surface, dislocations, or impurities). The increase of emitting centers in the host increases the emission intensity but also enhances the interaction of their excited states. The probability of interaction with luminescence killers also increases, thus resulting in a nonradiative de-excitation. This effect is called concentration quenching. The literature shows a wide range (from 12.5 to 30 mol %) of critical Eu^{3+} concentrations that give rise to maximum emission intensity in Eu:LaF_3 phosphors.[27−29] To find the precise Eu^{3+} content producing the maximum emission intensity in our Eu:LaF_3 system, luminescence spectra of the LaF_3 NPs doped with different Eu^{3+} concentrations were recorded. Figure 5a shows the excitation spectrum of the 20Eu:LaF_3 NPs recorded while monitoring the characteristic Eu^{3+} emission at 589 nm. The spectrum shows excitation peaks corresponding to 4f electronic transitions of Eu^{3+}, the most intense peaks appearing at 396 nm ($^7F_0 \rightarrow {}^5L_6$) in agreement with the literature.[30] The emission spectra obtained while exciting the Eu:LaF_3 samples at 396 nm (Figure 5b) show the characteristic emission bands of Eu^{3+}, including $^5D_0-{}^7F_1$ (589 nm), $^5D_0-{}^7F_2$ (612 nm), and $^5D_0-{}^7F_3$ (692 nm). The magnetic dipole transition at 589 nm is more intense than the electric dipole transition at 612 nm, which suggests the location of Eu^{3+} ions in crystallographic sites without an inversion center, in good agreement with the literature.[30] It can be observed in Figure 5b that the emission intensity increases with increasing Eu-doping level up to 20%, while increasing the Eu content to 30% decreases the emission intensity because of the concentration quenching effect.[31] The evolution of emission intensity with Eu doping level is more easily observed in the inset of Figure 5b, where the area under the curve of the emission spectra has been plotted versus Eu^{3+} concentration. The optimum Eu doping level to obtain maximum emission in our Eu:LaF_3 NPs is 20%, which is inside the interval found in the literature described above.

To confirm the presence of such concentration quenching effect, the decay curves of the samples have been recorded for

DOI: 10.1021/acsomega.8b03160
ACS Omega 2019, 4, 765−774

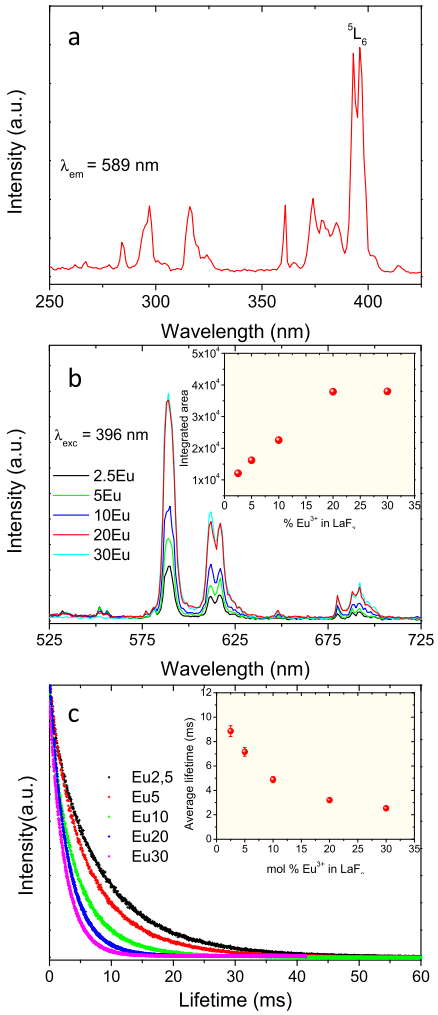

Figure 5. (a) Excitation spectrum of LaF_3 NPs doped with 20 mol % Eu^{3+} recorded while monitoring the Eu^{3+} emission at 589 nm. (b) Emission spectra of LaF_3 NPs doped with different Eu^{3+} contents, recorded at an excitation wavelength of 396 nm. The inset represents the integrated area (in the 525−725 nm interval) of the emission spectra vs the Eu content. (c) Temporal evolution of the $^5D_0 \rightarrow {}^7F_1$ luminescence (589 nm) for the LaF_3 NPs with increasing amounts of Eu^{3+} (excitation at 396 nm). The inset is a plot of the average lifetimes $\langle\tau\rangle$ calculated from the right hand-side term of eq 2, using the corresponding fitting parameters given in Table 1, vs Eu content.

the $^5D_0 \rightarrow {}^7F_1$ transition (589 nm), after pulsed excitation at λ_{ex} = 396 nm (Figure 5c). All curves could be successfully fitted to a biexponential decay function according to eq 1

$$I(t) = I_1 \exp(-t/\tau_1) + I_2 \exp(-t/\tau_2) \quad (1)$$

where $I(t)$ is the luminescence intensity, t is the time after excitation, and τ_i (i = 1, 2) is the decay time of the i component, with intensity I_i. The corresponding fitting parameters are summarized in Table 1 along with the average decay times, $\langle\tau\rangle$, defined as

$$\langle\tau\rangle = \frac{\int_{t_0}^{t_f} tI(t)\,dt}{\int_{t_0}^{t_f} I(t)\,dt} = (\tau_1^2 I_1 + \tau_2^2 I_2)/(\tau_1 I_1 + \tau_2 I_2) \quad (2)$$

The long lifetime has classically been assigned to the luminescent centers located in the interior of the NP, whereas the short lifetime values correspond to the surface ions, where

Table 1. Partial and Average Lifetimes Values for the Eu:LaF_3 NPs Obtained for the $^5D_0-{}^7F_1$ Transition (589 nm) after Pulsed Excitation (λ_{ex} = 396 nm) as a Function of the Eu Content

% Eu	t_1 (ms)	A_1 (%)	t_2 (ms)	A_2 (%)	T_{avg} (ms)
2.5	2.12	20	9.23	80	8.83
5	2.06	30	7.49	70	6.92
10	2.37	47	5.85	53	4.92
20	1.70	29	3.50	71	3.20
30	1.17	3	2.55	97	2.53

the presence of impurities, such as hydroxyl species, act as luminescence quenchers, thus increasing the decay rate.[32] The average lifetime values are plotted in the inset of Figure 5c versus Eu^{3+} content. It can be observed that the lifetimes decrease exponentially with increasing Eu^{3+} content from 2.5%, indicating that this is the most efficient composition. The observed increase in emission intensity with increasing Eu content up to 20% Eu^{3+} must therefore be assigned to the increase in emission centers that compensate the concentration quenching observed at much lower Eu^{3+} doping levels. Given that the maximum emission intensity is pursuit in this study, we have selected the 20Eu:LaF_3 sample for further codoping with Bi^{3+} ions.

2.2.2. Luminescence Characteristics of Bi^{3+} Ions in Bi^{3+}:LaF_3 NPs. To understand the energy transfer from Bi^{3+} to Eu^{3+} that will be analyzed later in this work for our Bi,Eu:LaF_3 system, we need to first analyze the excitation and emission spectra of Bi^{3+} in Bi-doped LaF_3 NPs. It is well-known that Bi^{3+} ions have an outer $6s^2$ electronic configuration with a ground state of $^1S_0$, whereas the excited states have 6s6p configuration and are split into the $^3P_0$, $^3P_1$, $^3P_2$, and $^1P_1$ levels (in sequence of increasing energy). Transitions between $^1S_0$ and $^3P_0$, and $^3P_2$ are spin forbidden. However, the $^3P_1$ level undergoes mixing with $^1P_1$ by spin−orbit coupling, allowing the $^1S_0 \rightarrow {}^3P_1$ and $^1S_0 \rightarrow {}^1P_1$ transitions. Symmetry of the local field at the Bi^{3+} ion strongly influences the relaxed excited states of the sp configuration and, therefore, the position of the excitation and emission bands of the Bi^{3+} strongly depends on the host lattice. A wide range of energy maxima for the Bi^{3+} excitation band have been reported in the literature, from 240 nm in Bi:$LaPO_4$ crystals[33] to 308 nm for Bi:$LaGaO_3$ perovskite.[34] Although the excitation and emission spectra of Bi^{3+} ions have been reported in the literature for a large number of host matrices,[9,14,34,35] the reports on fluoride matrices are really scarce[36] and, to the best of our knowledge, there is just one study about the luminescence of Bi^{3+} in a rare-earth fluoride matrix ($NaYF_4$),[37] where the energy maxima for the Bi^{3+} excitation band is reported at 248 nm. The excitation spectrum of 10%Bi:LaF_3 NPs (Figure 6a) shows a unique band rising at 275 nm with a maximum at λ < 250 nm, the minimum wavelength of our detector, which is in agreement with the value given in the literature for Bi:$NaYF_4$. The emission spectrum of the same sample, recorded under excitation at 250 nm, shows (Figure 6b) a broad band in the visible region of the spectrum that can be successfully fitted to a unique Gaussian function with the maximum at 520 nm. The unique band indicates a unique local field at the Bi^{3+} ion, and it is compatible with Bi^{3+} substituting La in the unique La site of the LaF_3 crystal structure.

2.2.3. Enhancement of Eu^{3+} Emission by Energy Transfer from Bi^{3+} to Eu^{3+} in Bi^{3+},Eu^{3+}:LaF_3 NPs. The emission spectra

DOI: 10.1021/acsomega.8b03160
ACS Omega 2019, 4, 765−774

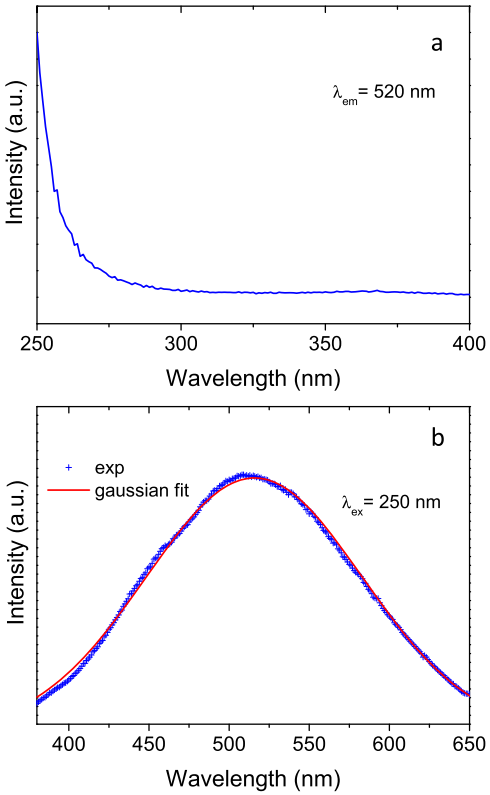

Figure 6. (a) Excitation spectrum of LaF_3 NPs doped with 10 mol % Bi^{3+} recorded while monitoring the emission of Bi^{3+} at 520 nm. (b) Blue crosses: Emission spectrum of LaF_3 NPs doped with 10 mol % Bi^{3+} recorded at an excitation wavelength of 250 nm. Red line: Gaussian fit to the emission spectrum.

of the *x*Bi,20Eu:LaF_3 NPs under excitation at 396 nm (direct Eu^{3+} excitation) are shown in Figure 7a. They exhibit the characteristic Eu^{3+} transitions, including $^5D_0-^7F_1$ (589 nm), $^5D_0-^7F_2$ (612 nm), and $^5D_0-^7F_3$ (692 nm). The intensity of all of the spectra, including that of the Bi-free sample, is identical as expected from the same number of Eu^{3+} emitting centers in all samples. When the excitation spectrum of any of the Bi-containing samples is recorded while monitoring the characteristic Eu^{3+} emission at 589 nm, the bands corresponding to the direct excitation of Eu^{3+} ions appear as a set of very weak bands at $\lambda > 280$ nm, whereas a very prominent band can be observed in the high-frequency region of the spectrum with maximum at $\lambda < 250$ nm (Figure 7b). This band is absent in the spectrum of the Bi-free sample and is, in turn, very similar to the excitation band of Bi:LaF_3 (Figure 6a). The observation of the Bi^{3+} excitation band while monitoring an Eu^{3+} emission in the Bi,Eu:LaF_3 NPs suggests the existence of an energy-transfer process from Bi^{3+} to Eu^{3+} in these samples. Figure 7c shows the emission spectra of the *x*Bi,20EuLaF$_3$ NPs recorded under excitation through the $Bi^{3+}\rightarrow Eu^{3+}$ energy transfer band (250 nm). The spectrum corresponding to the Bi-free sample is not shown because no emission is obtained under 250 nm for this composition, in agreement with the corresponding excitation spectrum. All spectra in Figure 7c show the same set of Eu^{3+} emission bands observed in Figure 7a, which confirms that the excitation band at 250 nm is due to a $Bi^{3+}\rightarrow Eu^{3+}$ energy-transfer process. Figure 7c also shows that the Eu^{3+} emission intensity increases with the increasing Bi^{3+} content. The area under the curve of the spectra in Figure 7c has been plotted, versus the Bi content, in Figure 7d, which also shows the intensity of the Bi-free sample under excitation at 396 nm. A significant increase in the emission intensity of more than 1

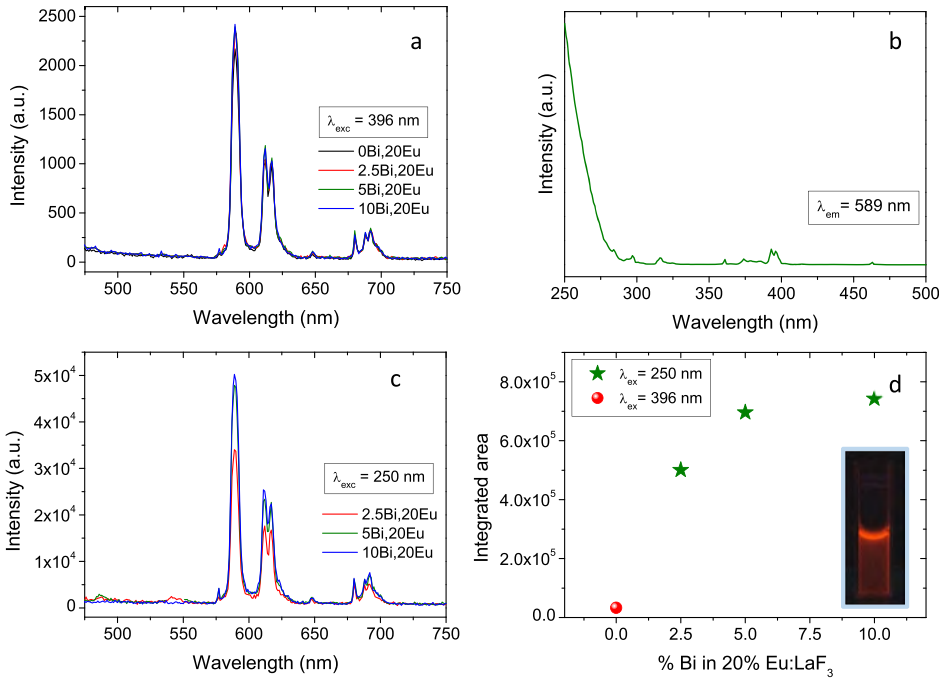

Figure 7. (a) Emission spectra of LaF_3 NPs doped with 20 mol % Eu^{3+} and different Bi^{3+} contents, recorded at an excitation wavelength of 396 nm (direct Eu^{3+} excitation). (b) Excitation spectrum of 10Bi,20Eu:LaF_3 and 0Bi,20Eu: LaF_3 NPs recorded while monitoring the Eu^{3+} emission at 589 nm. (c) Emission spectra of LaF_3 NPs doped with 20 mol % Eu^{3+} and different Bi^{3+} contents, recorded at an excitation wavelength of 250 nm ($Bi^{3+}\rightarrow Eu^{3+}$ energy-transfer band). (d) Integrated area (between 475 and 750 nm) of the spectra shown in (c) vs Bi^{3+} content. The red ball is the integrated area of the spectrum recorded under excitation at 396 nm on the Bi-free sample (shown in a). The inset is a photograph showing the intense red emission of an aqueous dispersion of 10Bi,20Eu:LaF_3 NPs under 250 nm irradiation.

DOI: 10.1021/acsomega.8b03160
ACS Omega 2019, 4, 765−774

order of magnitude is observed for the 2.5B,20Eu:LaF_3 sample in comparison with the Bi-free sample. The intensity of the spectra continues increasing with the increasing Bi content from 2.5 to 5%, whereas it plateaus at 10%, which is possibly because of Bi^{3+} concentration-quenching effect. The intense red emission of an aqueous dispersion of this sample under 250 nm irradiation can be observed in the inset of Figure 7d. It can then be concluded that it is possible to significantly increase the emission intensity of Eu:LaF_3 NPs by codoping with Bi^{3+} ions, thanks to the Bi → Eu energy-transfer process, the maximum emission being observed for the 10Bi,20Eu:LaF_3 sample.

Finally, to know the mechanism governing the Bi → Eu energy-transfer process in Bi,Eu-codoped LaF_3 NPs, the following analysis has been carried out. It is well-known that there are two main mechanisms for energy transfer, namely radiative transfer and nonradiative transfer.[38] The former involves emission of the sensitizer (Bi^{3+}) and reabsorption by the activator (Eu^{3+}). The efficiency of radiative transfer requires a significant overlap of the emission region of the sensitizer and the absorption region of the activator and an appreciable intensity of the absorption of the latter. To check if the requirements for radiative transfer are satisfied in our system, we have plotted in Figure 8 the excitation spectrum of

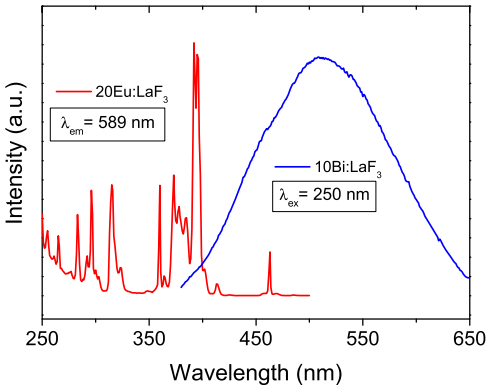

Figure 8. Red: Excitation spectrum of 20Eu:LaF_3 monitored at an emission wavelength of 589 nm, corresponding to the maximum emission intensity of Eu^{3+}. Blue: Emission spectrum of 10Bi:LaF_3 recorded under an excitation wavelength of 250 nm, corresponding to the maximum excitation of Bi^{3+}.

20Eu:LaF_3 NPs (monitored at 589 nm) and the emission spectrum of 10Bi:LaF_3 NPs (recorded under an excitation wavelength of 250 nm). A negligible overlap between the main excitation band of Eu^{3+} and the emission of Bi^{3+} can be observed. From this observation, it is possible to conclude that the Bi^{3+} → Eu^{3+} energy transfer in Bi,Eu:LaF_3 system is nonradiative in character, as is the case in many inorganic systems.[38]

2.3. X-ray Attenuation Capacity of Eu^{3+}:LaF_3 NPs: Effect of Bi^{3+} Codoping. Figure 9 (top) shows the X-ray attenuation capacity (in HU units) of aqueous suspensions of 20Eu:LaF_3 NPs and 10Bi,20 Eu:LaF_3 NPs versus concentration of the suspensions. The HU values for iohexol, a clinically used, iodine-based CT contrast agent, are also shown. It can be observed that the HU values increase linearly with increasing the concentration of the aqueous suspensions of the three types of compounds. The slope of the curve corresponding to 20Eu:LaF_3 is about 23.4, which is higher

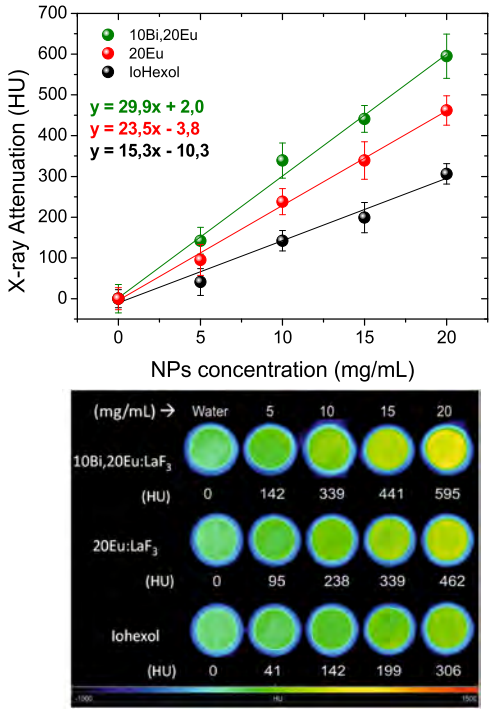

Figure 9. Top: X-ray attenuation values, in Hounsfield units, of aqueous suspensions of 10Bi,20Eu:LaF_3 NPs (green circles), 20Eu:LaF_3 NPs (red circles), and iohexol (black circles), vs concentration of their suspensions. Lines are linear fits to the data; the corresponding equations are shown as well. Bottom: In vitro X-ray CT images of aqueous suspensions of 10Bi,20Eu:LaF_3 NPs, 20Eu:LaF_3 NPs, and iohexol at different concentrations.

than that of iohexol (15.3), whereas the 20Eu,10Bi:LaF_3 NPs show the highest slope (29.9). The difference in attenuation among the three different materials can be easily appreciated in Figure 9 (bottom), which shows the X-ray images of each suspension. The increase in X-ray attenuation capacity of the Bi-containing LaF_3 NPs with respect to those just doped with Eu is in agreement with the equation defining the X-ray absorption coefficient (μ) of any material: $\mu = (\rho Z^4)/(AE^3)$, where ρ is the density, Z is the atomic number, A is the atomic mass, and E is the X-ray energy. The higher atomic number of Bi (Z = 83) compared with La (Z = 57) increases the absorption coefficient and therefore, the CT value of the 20Eu,10Bi:LaF_3 suspensions. The HU values obtained for 10Bi,20Eu:LaF_3 at any concentration of the suspension are more than double those of iohexol, which allows using a lower dose of contrast agent, with a consequent benefit to the patient. The 20Eu,10Bi:LaF_3 NPs are therefore excellent candidates as contrast agents for X-ray CT.

2.4. Cytotoxicity Assay. The 3-(4,5-dimethylthiazol-2-yl)-2,5-diphenyltetrazolium bromide (MTT) colorimetric assay was used to determine the cytotoxicity of the 10Bi,20Eu:LaF_3 NPs using Vero cells which were incubated with NP suspensions of different concentrations for 24 h. Figure 10 indicates that NPs showed negligible toxicity effects with viability percentages as high as 80% for concentrations up to 0.1 mg·mL^{-1}, thus fulfilling the biocompatibility criteria required for bioapplications.

DOI: 10.1021/acsomega.8b03160
ACS Omega 2019, 4, 765−774

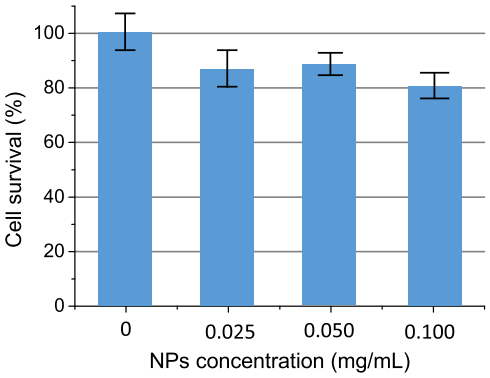

Figure 10. Cytotoxicity profiles for Vero cells incubated with different concentrations of 10Bi,20Eu:LaF_3 NPs for 24 h. The percentage viability of the cells is expressed relative to that of control cells.

3. CONCLUSIONS

Uniform, nonaggregated LaF_3 NPs, singly doped with Eu^{3+} and codoped with Eu^{3+} and Bi^{3+}, can be obtained using a simple and quick method at room temperature and in just 2 h. The method consists of the aging of an EG−water solution containing La^{3+}, Eu^{3+}, and Bi^{3+} nitrates, in stoichiometric amounts, and $NaBF_4$, which slowly releases fluoride ions by hydrolysis, thus allowing the homogeneous precipitation of the fluoride salt. The analysis of the luminescence of singly Eu^{3+}−doped LaF_3 NPs demonstrated that the 20 mol % Eu content produced the highest emission intensity. Codoping the 20 mol % Eu^{3+} LaF_3 NPs with Bi^{3+} allowed excitation of the NPs through the $Bi^{3+} \rightarrow Eu^{3+}$ energy-transfer band, which enhanced the emission intensity in more than 1 order of magnitude, the higher emission being obtained for the NPs codoped with 20 mol % Eu^{3+} and 10 mol % Bi^{3+}. The presence of bismuth in the NP composition was beneficial as well to increase the X-ray attenuation capacity of the material because of the high atomic number of Bi. The codoped NPs demonstrated cell viability at concentrations up to 0.1 mg/mL. This feature, together with their excellent luminescent and X-ray attenuation properties, makes these NPs potential bimodal candidates as luminescent bioprobes and contrast agents for optical bioimaging and X-ray CT, respectively. In addition, the facile and fast synthesis method allows the preparation of NPs on a large scale, in contrast with other methods reported in the literature that demand complex equipment for hydrothermal or solvothermal synthesis.

4. MATERIALS AND METHODS

4.1. Materials. EG (anhydrous, Sigma Aldrich, 99.8%), lanthanum nitrate ($La(NO_3)_3{\cdot}6H_2O$, Sigma-Aldrich, 99%), europium nitrate hydrate ($Eu(NO_3)_3{\cdot}xH_2O$, Sigma-Aldrich, 99.9%), bismuth nitrate ($Bi(NO_3)_3{\cdot}5H_2O$, Sigma-Aldrich, 99.9%), sodium tetrafluoroborate (NaBF4, Sigma-Aldrich, 98%) were used as received.

4.2. Synthesis of Samples. Eu-doped LaF_3 NPs were obtained according to the following method: lanthanum nitrate and europium nitrate were dissolved in 3 mL of an EG−water (EG/H_2O) mixture (90/10 v/v). The lanthanide ion (La + Eu) concentration was kept constant (0.1 mol·dm^{-3}) in all experiments, whereas the Eu/(La + Eu) molar ratio was varied from 2.5 to 30%. Sodium tetrafluoroborate was separately dissolved in 3 mL of EG/H_2O mixture (90/10 v/v) at room temperature with magnetic stirring for 2 h to obtain the $NaBF_4$ concentration of 1.44 mol·dm^{-3}. Both solutions were admixed together and aged at room temperature for 2 h in glass tubes. The resulting suspension was centrifuged to remove the supernatants, and the precipitates were washed with ethanol and distilled water. For some analyses, the precipitates were dried at room temperature.

Eu,Bi codoped LaF_3 NPs were synthesized following the same procedure and using bismuth nitrate hydrate as the Bi^{3+} source. A fixed Eu^{3+} doping level of 20 mol % was used for the synthesis, whereas the Bi^{3+} content was varied from 2.5 to 10 mol %. Finally, 10% Bi-doped LaF_3 NPs were also synthesized using the same protocol.

4.3. Characterization Techniques. Transmission electron microscopy (TEM, Philips 200CM) was used to examine the particle morphology. Particle size distribution was obtained from TEM micrographs by measuring a hundred of particles with the free software *ImageJ*. DLS in a Malvern Zetasizer Nano-ZS90 equipment was used to get information on the size of the particles in aqueous suspension and to detect particle aggregation in suspension, if any. The experiments were carried out using aqueous suspensions of the particles at a concentration of 0.5 mg·mL^{-1}. The same equipment was used to measure the zeta potential of the particles. The crystalline structure of the particles was examined by XRD using a Panalytical, X'Pert Pro diffractometer (Cu Kα) with an X-Celerator detector over an angular range of $10° < 2\theta < 120°$ 2θ, 0.02° step width, and 10 s counting time. Silicon was used as an internal standard. Lattice parameters of the LaF_3 crystal structure were calculated using the Rietveld method with the TOPAS software (TOPAS version 4.2, Bruker AXS, 2009). The following parameters were refined: background coefficients, zero of the diffractometer, scale factor, lattice parameters, displacement parameters of La^{3+}, and profile parameters. The isomorphic substitution of Eu^{3+} and/or Bi^{3+} by La^{3+} in LaF_3 was proved in comparison with the lattice parameters of the undoped NPs with both Eu^{3+}- and Bi^{3+}-doped materials.

The *excitation and emission spectra* of Eu^{3+}-doped, Bi^{3+}-doped, and Eu^{3+},Bi^{3+}-codoped LaF_3 NPs dispersed in water (0.5 mg·mL^{-1}) were measured in a Horiba Jobin Yvon spectrofluorimeter (Fluorolog3). Excitation and emission slits used to record excitation spectra were 1 and 5 nm, respectively, whereas they were turned to 5 and 1 nm, respectively, when the emission spectra were recorded. In both cases, a step size of 1 nm was used. All spectra were lamp-and-detector-corrected using corrections files provided with the fluorimeter. Luminescence decay curves associated to the $^5D_0 - {}^7F_1$ transition of Eu^{3+} (λ_{em} = 589 nm) were recorded using a pulse lamp installed in the same fluorimeter.

CT contrast efficiency was evaluated in a NanoSPECT/CT (Bioscan). Aqueous dispersions containing different concentrations of the NPs in Eppendorf tubes were placed in a multiwell microplate, along with a Milli-Q water sample for calibration. Images were then acquired for 18 min using the following parameters: 106 mA current for a voltage of 75 kV, exposure time per projection of 1500 ms, and 360 projections per rotation. The image length was 6 cm, with a pitch of 1. Images were reconstructed with Vivoquant image processing software (Invicro) and subsequently analyzed using the PMOD 3.8 software (PMOD Technologies LLC). Spherical volumes of interest (2 mm radius) were made within each sample to calculate the X-ray attenuation for each concentration in Hounsfield units (HU).

DOI: 10.1021/acsomega.8b03160
ACS Omega 2019, 4, 765−774

Cell viability was determined using an MTT colorimetric assay. Vero cells (kidney epithelial cells isolated from African green monkey, ATCC number CCL-81) were grown at 37 °C in a 5% CO_2 atmosphere in Dulbecco's modified Eagle's medium (DMEM) supplemented with 10% fetal bovine serum, penicillin (100 U/mL), streptomycin (100 μg/mL), and glutamine (2 mM). Cells (7500) were seeded using standard 96-well culture plates and cultured for 24 h. The medium was then replaced with new one containing the NPs at different concentrations (0.025, 0.05, and 0.1 mg/mL) and a negative control containing no NPs (nontreated cells). Five replicates were performed per sample. After 24 h of incubation, cells were thoroughly washed with DPBS and incubated with fresh medium containing the MTT dye solution (0.5 mg/mL in DMEM). Following 2 h of incubation at 37 °C, formazan salts were dissolved with 200 μL of dimethyl sulfoxide, and the absorbance (Abs) was determined at λ = 570 nm on a microplate reader (Thermo Scientific Multiskan GO UV/vis microplate spectrophotometer). The relative cell viability (%) of control cells without NPs was calculated from the ratio between the Abs of the sample and that of the control. Experiments were carried out in duplicate.

■ ASSOCIATED CONTENT

Supporting Information

The Supporting Information is available free of charge on the ACS Publications website at DOI: 10.1021/acsomega.8b03160.

SEM micrographs of LaF_3 NPs doped with different Eu^{3+} contents and codoped with 20 mol % Eu and different Bi^{3+} contents (PDF).

■ AUTHOR INFORMATION

Corresponding Author

*E-mail: anieto@icmse.csic.es.

ORCID

Ana Isabel Becerro: 0000-0003-2243-5438

Manuel Ocaña: 0000-0001-9989-606X

Notes

The authors declare no competing financial interest.

■ ACKNOWLEDGMENTS

We gratefully acknowledge T.C. Rojas for help with TEM. This work was supported by CSIC projects (PIC2016FR1 and PIE201460E005), Fondo Social Europeo-Gobierno de Aragón and by Siemens Healthcare S.L.U. We acknowledge the use of the CNA's ICTS NanoCT facilities.

■ REFERENCES

(1) Shen, J.; Sun, L.-D.; Yan, C.-H. Luminescent rare earth nanomaterials for bioprobe applications. *Dalton Trans.* **2008**, 5687−5697.

(2) Wang, G.; Peng, Q.; Li, Y. Lanthanide-Doped Nanocrystals: Synthesis, Optical-Magnetic Properties, and Applications. *Acc. Chem. Res.* **2011**, *44*, 322−332.

(3) Li, C.; Lin, J. Rare earth fluoride nano-/microcrystals: synthesis, surface modification and application. *J. Mater. Chem.* **2010**, *20*, 6831−6847.

(4) Geng, D.; Lozano, G.; Calvo, M. E.; Núñez, N. O.; Becerro, A. I.; Ocaña, M.; Míguez, H. Photonic Tuning of the Emission Color of Nanophosphor Films Processed at High Temperature. *Adv. Opt. Mater.* **2017**, *5*, 1700099.

(5) Laguna, M.; Núñez, N. O.; Garcia, F. J.; Corral, A.; Parrado-Gallego, Á.; Balcerzyk, M.; Becerro, A. I.; Ocaña, M. Microemulsion-Mediated Synthesis and Properties of Uniform Ln:CaWO4 (Ln = Eu, Dy) Nanophosphors with Multicolor Luminescence for Optical and CT Imaging. *Eur. J. Inorg. Chem.* **2017**, 5158−5168.

(6) Laguna, M.; Escudero, A.; Núñez, N. O.; Becerro, A. I.; Ocaña, M. Europium-doped NaGd(WO4)2 nanophosphors: synthesis, luminescence and their coating with fluorescein for pH sensing. *Dalton Trans.* **2017**, *46*, 11575−11583.

(7) Laguna, M.; Nuñez, N. O.; Becerro, A. I.; Ocaña, M. Morphology control of uniform CaMoO4microarchitectures and development of white light emitting phosphors by Ln doping (Ln = Dy3+, Eu3+). *CrystEngComm* **2017**, *19*, 1590−1600.

(8) Becerro, A. I.; Allix, M.; Laguna, M.; González-Mancebo, D.; Genevois, C.; Caballero, A.; Lozano, G.; Núñez, N. O.; Ocaña, M. Revealing the substitution mechanism in Eu3+:CaMoO4 and Eu3+,Na+:CaMoO4 phosphors. *J. Mater. Chem. C* **2018**, *6*, 12830−12840.

(9) Li, K.; Lian, H.; Shang, M.; Lin, J. A novel greenish yellow-orange red Ba3Y4O9:Bi3+,Eu3+ phosphor with efficient energy transfer for UV-LEDs. *Dalton Trans.* **2015**, *44*, 20542−20550.

(10) Wang, Y.; Wu, C.; Wei, J. Hydrothermal synthesis and luminescent properties of LnPO4:Tb,Bi (Ln=La,Gd) phosphors under UV/VUV excitation. *J. Lumin.* **2007**, *126*, 503−507.

(11) Hussain, S. K.; Bharat, L. K.; Kim, D. H.; Yu, J. S. Facile pechini synthesis of Sr 3 Y 2 Ge 3 O 12 :Bi 3+/Eu 3+ phosphors with tunable emissions and energy transfer for WLEDs. *J. Alloys Compd.* **2017**, *703*, 361−369.

(12) Huang, A.; Yang, Z.; Yu, C.; Chai, Z.; Qiu, J.; Song, Z. Tunable and White Light Emission of a Single-Phased $Ba_2Y(BO_3)_2Cl$:Bi^{3+},Eu^{3+} Phosphor by Energy Transfer for Ultraviolet Converted White LEDs. *J. Phys. Chem. C* **2017**, *121*, 5267−5276.

(13) Hussain, S. K.; Yu, J. S. Sol-gel synthesis of Eu 3+/Bi 3+ ions co-doped BaLa 2 WO 7 phosphors for red-LEDs under NUV excitation and FEDs applications. *J. Lumin.* **2017**, *183*, 39−47.

(14) Wangkhem, R.; Yaba, T.; Shanta Singh, N.; Ningthoujam, R. S. Red emission enhancement from CaMoO4:Eu3+ by co-doping of Bi3+ for near UV/blue LED pumped white pcLEDs: Energy transfer studies. *J. Appl. Phys.* **2018**, *123*, 124303.

(15) Lenczewska, K.; Gerasymchuk, Y.; Vu, N.; Liem, N. Q.; Boulon, G.; Hreniak, D. The size effect on the energy transfer in Bi3+-Eu3+ co-doped GdVO4 nanocrystals. *J. Mater. Chem. C* **2017**, *5*, 3014−3023.

(16) Lei, F.; Zou, X.; Jiang, N.; Zheng, Q.; Lam, K. H.; Luo, L.; Ning, Z.; Lin, D. Regulated morphology/phase structure and enhanced fluorescence in YF3:Eu3+,Bi3+via a facile method. *CrystEngComm* **2015**, *17*, 6207−6218.

(17) Lusic, H.; Grinstaff, M. W. X-ray-Computed Tomography Contrast Agents. *Chem. Rev.* **2012**, *113*, 1641.

(18) Park, J.; An, K.; Hwang, Y.; Park, J.-G.; Noh, H.-J.; Kim, J.-Y.; Park, J.-H.; Hwang, N.-M.; Hyeon, T. Ultra-large-scale syntheses of monodisperse nanocrystals. *Nat. Mater.* **2004**, *3*, 891−895.

(19) Johnson, N. J. J.; Oakden, W.; Stanisz, G. J.; Scott Prosser, R.; van Veggel, F. C. J. M. Size-Tunable, Ultrasmall NaGdF4Nanoparticles: Insights into Their T1MRI Contrast Enhancement. *Chem. Mater.* **2011**, *23*, 3714−3722.

(20) González-Mancebo, D.; Becerro, A. I.; Rojas, T. C.; Olivencia, A.; Corral, A.; Balcerzyk, M.; Cantelar, E.; Cussó, F.; Ocaña, M. Room temperature synthesis of water-dispersible Ln 3+ :CeF 3 (Ln = Nd, Tb) nanoparticles with different morphology as bimodal probes for fluorescence and CT imaging. *J. Colloid Interface Sci.* **2018**, *520*, 134−144.

(21) Elmenoufy, A. H.; Tang, Y.; Hu, J.; Xu, H.; Yang, X. A novel deep photodynamic therapy modality combined with CT imaging established via X-ray stimulated silica-modified lanthanide scintillating nanoparticles. *Chem. Commun.* **2015**, *51*, 12247−12250.

(22) Liu, C.; Sun, J.; Wang, H.; Chen, D. Size and morphology controllable synthesis of oil-dispersible LaF3:Yb,Er upconversion

DOI: 10.1021/acsomega.8b03160
ACS Omega 2019, 4, 765−774

fluorescent nanocrystals via a solid-liquid two-phase approach. *Scr. Mater.* **2008**, *58*, 89−92.
(23) Sivakumar, S.; Diamente, P. R.; van Veggel, F. C. J. M. Silica-Coated Ln3+-Doped LaF3 Nanoparticles as Robust Down- and Upconverting Biolabels. *Chem.—Eur. J.* **2006**, *12*, 5878−5884.
(24) Yi, G.-S.; Chow, G.-M. Colloidal LaF3:Yb,Er, LaF3:Yb,Ho and LaF3:Yb,Tm nanocrystals with multicolor upconversion fluorescence. *J. Mater. Chem.* **2005**, *15*, 4460−4464.
(25) Matijevic, E. Preparation and properties of uniform size colloids. *Chem. Mater.* **1993**, *5*, 412−426.
(26) Feldmann, C. Polyol-Mediated Synthesis of Nanoscale Functional Materials. *Adv. Funct. Mater.* **2003**, *13*, 101−107.
(27) Pi, D.; Wang, F.; Fan, X.; Wang, M.; Zhang, Y. Luminescence behavior of Eu3+ doped LaF3 nanoparticles. *Spectrochim. Acta, Part A* **2005**, *61*, 2455−2459.
(28) Zhang, C.; Chen, J.; Zhou, Y.; Li, D. Ionic Liquid-Based ″All-in-One″ Synthesis and Photoluminescence Properties of Lanthanide Fluorides. *J. Phys. Chem. C* **2008**, *112*, 10083−10088.
(29) Wang, Z.; Li, M.; Wang, C.; Chang, J.; Shi, H.; Lin, J. Photoluminescence properties of LaF3: Eu3+ nanoparticles prepared by refluxing method. *J. Rare Earths* **2009**, *27*, 33.
(30) Lorbeer, C.; Mudring, A.-V. White-Light-Emitting Single Phosphors via Triply Doped LaF3 Nanoparticles. *J. Phys. Chem. C* **2013**, *117*, 12229−12238.
(31) Fernández-Carrión, A. J.; Ocaña, M.; García-Sevillano, J.; Cantelar, E.; Becerro, A. I. New Single-Phase, White-Light-Emitting Phosphors Based on *δ*-Gd2Si2O7 for Solid-State Lighting. *J. Phys. Chem. C* **2014**, *118*, 18035−18043.
(32) Stouwdam, J. W.; van Veggel, F. C. J. M. Near-infrared Emission of Redispersible Er3+, Nd3+, and Ho3+Doped LaF3Nanoparticles. *Nano Lett.* **2002**, *2*, 733−737.
(33) Moncorge, R.; Boulon, G.; Denis, J.-P. Fluorescence properties of bismuth-doped LaPo4. *J. Phys. C: Solid State Phys.* **1979**, *12*, 1165−1171.
(34) Srivastava, A. M. Luminescence of Bi3+ in LaGaO3. *Mater. Res. Bull.* **1999**, *34*, 1391−1396.
(35) Dang, P.; Liang, S.; Li, G.; Wei, Y.; Cheng, Z.; Lian, H.; Shang, M.; Ho, S. J.; Lin, J. Controllable optical tuning and improvement in Li+,Eu3+-codoped BaSc2O4:Bi3+ based on energy transfer and charge compensation. *J. Mater. Chem. C* **2018**, *6*, 6449−6459.
(36) Oboth, K. P.; Lohmeier, F. J.; Fischer, F. VUV and UV Spectroscopy of Pb2+ and Bi3+ Centres in Alkaline-Earth Fluorides. *Phys. Status Solidi B* **1989**, *154*, 789−803.
(37) Chong, K.; Hirai, T.; Kawai, T.; Hashimoto, S.; Ohno, N. Optical properties of Bi3+ ions doped in NaYF4. *J. Lumin.* **2007**, *122−123*, 149−151.
(38) Blasse, G.; Bril, A. Study of Energy Transfer from Sb3+, Bi3+, Ce3+ to Sm3+, Eu3+, Tb3+, Dy3+. *J. Chem. Phys.* **1967**, *47*, 1920−1926.

DOI: 10.1021/acsomega.8b03160
ACS Omega 2019, 4, 765−774